Structural analysis of biomass pyrolysis and oxidation using *in-situ* X-ray computed tomography

Emeric Boigné [a,*], N. Robert Bennett [b], Adam Wang [b], Matthias Ihme [a]

[a] *Department of Mechanical Engineering, Stanford University, Stanford, CA 94305, United States*
[b] *Department of Radiology, Stanford University, Stanford, CA 94305, United States*

ARTICLE INFO

ABSTRACT

Detailed measurements are performed to examine the heterogeneous processes that occur within the solid fuel during the combustion of biomass. Specifically, the pyrolysis, char oxidation, and volume shrinkage are examined using X-ray computed tomography (XCT). Simultaneous 3D *in-situ* measurements of solid density and gas-phase temperature are acquired at a spatial resolution of 300 μm for 1.6-cm size samples of birch, douglas fir, oak and walnut. To simultaneously measure the heterogeneous combustion processes and the gas-phase temperature, the flow is doped with Kr, a high X-ray contrast agent. By varying the molar oxygen concentration from 0% to 21%, regimes of pyrolysis, smoldering, and flaming are identified for different types of biomass and grain orientations. Results from these multidimensional XCT measurements provide new insights about the fuel volume reduction, from which shrinkage parameters are experimentally determined. The simultaneous acquisition of gas-phase temperature measurements also highlights the direct dependence of flame anchoring upon grain orientation. In addition, the char oxidation is found to be limited to a narrow region with 2 mm thickness at the smoldering surface, while the propagation of the pyrolysis front is measured up to 1 cm within the sample. For some biomass materials, significant density fluctuations are measured at the millimeter scale, indicating non-homogeneous reaction rates.

1. Introduction

Biomass combustion is encountered in applications involving energy production and wildfires. Biomass remains the largest renewable energy source, with solid biomass contributing to about 60% of the total energy production from renewable sources [1]. The combustion of biomass is also relevant in the context of wildfires, a growing natural activity that threatens to accelerate climate change. In particular, because of increasing fire activity, climate conditions are increasingly unsuitable for forest regeneration [2], and boreal forest soils are expected to transition from being a historical sink of carbon to becoming a source of carbon [3]. In addition, biomass pyrolysis and smoldering is relevant in waste treatment [4,5], soil remediation [6], and traditional fluidized bed reactors, for which it remains difficult to provide quantitative predictions of product yields that are required for process design [7].

To address these environmental and industrial challenges, numerous studies have investigated the fundamental mechanisms of biomass combustion. Specifically, standardized testings of material properties have been established using cone calorimeters [8,9], thermogravimetric analyzers (TGA) [10,11], and custom reactors [12]. State-of-the-art models of biomass combustion represent the fuel composition as a mixture of water, cellulose, hemicellulose, and lignin, and account for thermal and oxidative pyrolyzates [13,14]. Other studies have investigated the role of unsteady flame dynamics in wildfire spread [15], the influence of moisture content on gas and particle emissions [16], the influence of oxygen concentration [17,18], sample size and shape on burning rates [19,20], as well as reaction quenching and extinction [21,22].

Besides, several studies have focused on the heterogeneous processes occurring within the solid fuel, revealing the importance of the internal dynamics. For instance, one internal mechanism fundamental to the pyrolysis is the volume shrinkage during char conversion. Neglecting the shrinkage can almost double predictions of char yield [23] or underpredict the pyrolysis rate by as much as 40% for samples large enough to exhibit spatial temperature variations [24]. In addition, studies have indicated that using realistic microstructure to model the heat and mass transfer within biomass samples is important to differentiate the intraparticle transport for different feedstocks [25]. Recent

---

* Corresponding author.
E-mail address: eboigne@stanford.edu (E. Boigné).

multiscale studies of wood smoldering concluded that chemistry and heat transfer are both important for the accurate prediction of the reaction fronts and burning rates [26]. These internal processes were modeled by considering simple configurations [27,28] and numerical simulations of biomass samples [13,14,19,26,29].

However, only a limited amount of experiments have reported detailed measurements of these internal dynamics. Several challenges can explain this lack of measurements, including the limitations in optical access, the requirements for high spatial and temporal resolution, and the difficulty in acquiring measurements inside the fuel while characterizing the gas-phase environment. Without further measurements, it remains difficult to understand fundamental internal mechanisms and develop accurate models. To provide such detailed measurements, *in-situ* ultrasound was employed to measure the permeability within a burning foam [30,31]. With 2D arrays of microphones a spatial resolution of 10 mm was achieved, and results highlighted the role of secondary char oxidation during the transition from smoldering to flaming. Alternatively, X-ray Computed Tomography (XCT) was used to image the gasification and combustion of coal *in-situ* [32–34] and the drying of wood [35]. Synchrotron XCT was also employed to characterize the cavity and ash formation in biomass pellets [36]. These studies revealed the potential of using XCT to capture internal combustion dynamics in dense and optically inaccessible samples.

XCT is a well established diagnostic method that has been extensively used in biological and material sciences to investigate solid samples and in medical applications. XCT enables 3D density field measurements at high spatial resolution, without suffering from optical limitations such as beam steering and limited depth of field. Even though the time resolution of XCT remains limited by the tomography rotation, advances in imaging hardware and reconstruction algorithms enable *in-situ* 3D measurements at up to 20 Hz [37], thus closing the gap towards enabling real-time XCT. Recent studies from different groups reported on using XCT to study biomass combustion, either to image wood pyrolysis [38] or water migration in wood vessels during imbibition [39]. Recently, a technique was proposed that combines XCT with Kr flow dilution to simultaneously measure the 3D fields of gas temperature and solid density during combustion [40]. This *in-situ* method was demonstrated by measuring the propagation speeds of pyrolysis and oxidation fronts for oak samples heated by a flame. The technique was later employed to evaluate the efficacy of fire retardants, highlighting a large suppression in char oxidation, but only a limited impact on the heat released during flaming [41].

To analyze the internal dynamics of biomass combustion and provide further detailed experimental measurements, the present study investigates the structural changes inside biomass samples using *in-situ* XCT with Kr flow dilution. Specifically, the first objective of this work is to provide fundamental insights and reference data by characterizing the internal combustion processes for different types of biomass. In particular, using 3D XCT measurements, the volume shrinkage and the reaction fronts of the pyrolysis and oxidation inside the fuel are examined in detail. A second objective is to investigate which are the dominant factors that affect fuel consumption at the meso-scale. Specifically, by comparing materials with similar micro-scale composition and chemical kinetics, this work investigates the impact on the combustion of the millimeter-scale fuel structure. Finally, a third objective is to further advance the capabilities of XCT as an *in-situ* method for providing reference measurements and guiding the development of heterogeneous combustion models. The accuracy of the XCT measurements is notably improved by considering the previously neglected attenuation of Kr inside the solid. To achieve these goals, four different biomass samples are characterized, and heated by a well-controlled radiation source in flows with 50% Kr dilution. The experimental setup enables the examination of an extended range of operating conditions, with oxygen concentrations ranging from 0% to 21% per volume. Using a laboratory system, *in-situ* XCT measurements are acquired to simultaneously measure the gas-phase temperature and the solid density during the transient combustion. The experimental method is presented in Section 2, and the setup is described in Section 3. Multidimensional results are reported in Section 4, along with an analysis of the internal pyrolysis and char oxidation. Section 5 presents the conclusions of this work.

2. Experimental method

2.1. X-ray absorption of biomass

In this work, X-ray absorption measurements were performed. X-ray photons interact with electrons on their trajectory, because of their sub-nanometer wavelengths. When encountering an electron, an X-ray photon can be scattered, or partially, or entirely absorbed. At the macroscopic scale, the attenuation of a beam of X-ray photons through matter is described by the Beer–Lambert law [42]. This law relates the attenuated intensity I to the incident intensity I_0 and the local linear attenuation value μ:

$$I = I_0 \exp \left(- \int \mu(l) \, dl \right) . \tag{1}$$

The linear attenuation is a function of material density, atomic composition, and photon energy. In the following, the dependence on the photon energy is eliminated by considering energy-integrated attenuation quantities [43]. As a result, the linear attenuation μ can be expressed as a function of material density ρ and atomic composition only

$$\mu = \rho \zeta , \tag{2}$$

in which ζ is the energy-integrated mass attenuation coefficient. For a given energy spectrum, this coefficient is only a function of the material composition, and can be expressed as

$$\zeta = \sum_{i=1}^{N_a} Y_i \zeta_i , \tag{3}$$

in which the summation is performed over the N_a atomic elements composing the specimen, where Y_i and ζ_i are the mass-fraction and energy-integrated mass attenuation coefficient of atomic element i, respectively. The mass attenuation coefficients are a function of atomic cross-sections, and tabulated values are available [44]. For biomass samples, the material consists mostly of H, C, and O atoms, whose mass fractions can be measured via ultimate analysis [10]. A theoretical mass attenuation coefficient for biomass ζ_b^{th} is therefore determined via Eq. (3), and compared to experimental measurements.

Biomass also contains minor amounts of N, S and ash. Ash consists of mineral oxides such as NaO_2, SiO_2, K_2O, or CaO. Because of the larger cross-sections of inorganic atoms, the mass attenuation coefficients of ash compounds can be up to ten times higher than those of organic matter. However, because the inorganic content accounts for less than 1% of the initial mass of the materials considered, its contribution to the X-ray attenuation inside the sample is neglected. Indeed, accounting for the contributions of the mineral atoms as well as N and S atoms modifies the value of ζ_b^{th} by less than 3% compared to what is obtained by considering H, C, and O atoms only. This error is thus within the uncertainty of the measurements. Further details on the attenuation of ashes and biomass are provided as supplementary material.

2.2. Volume shrinkage under pyrolysis

The combustion of biomass is a combination of the endothermic pyrolysis into char, and the exothermic oxidation of this char

to gaseous combustion products and solid ash. The pyrolysis reaction is associated with a volume shrinkage of the solid, and characterizing this effect is fundamental to accurately predict the reaction rates. This shrinkage can be particularly relevant in fluidized bed reactors with high mass loss levels, in which a large volume reduction can alter the effective thermal conductivity of particles and influence the overall yield [45]. Previous studies have highlighted that the volume shrinkage is a function of the effective rate of pyrolysis, and therefore of the heating rate [23,24,46]. Swelling of biomass was not observed in the present study, even though it can occur during pyrolysis because of thermal expansion and pressure increase within closed solid pores due to devolatilization [47]. When undergoing pyrolysis, an initial volume V_b of biomass will shrink into a volume V_c of char. From mass conservation, the ratio of the two volumes γ can be expressed as

$$\gamma = \frac{V_c}{V_b} = (1 - Y_p)\frac{\rho_b}{\rho_c} \ , \tag{4}$$

in which Y_p is the mass fraction of volatile gases released by the biomass during pyrolysis. Char shrinkage is frequently characterized using the fraction χ of bulk density difference between char and biomass that is converted to gases, written as [13,26,29]

$$\chi = \frac{1 - \gamma\rho_c/\rho_b}{1 - \rho_c/\rho_b} \ . \tag{5}$$

In 1D numerical models of pyrolysis and smoldering, the volume shrinkage is either neglected or modeled using a single constant value for the volumetric shrinkage ratio [13,29,45,48]. For instance, in a study using the Gpyro open-source code [13], a choice of $\gamma = 1.0$ was justified by fitting the numerical results to measurements. However, detailed experimental measurements of the present study suggest that a value of $\gamma = 0.675$, or $\chi = 1.28$ is more appropriate to represent the materials considered. Because XCT measurements enable the full 3D reconstruction of the sample density field, high-order methods, such as motion vector fields, could be used to further analyze the shrinkage and validate different models [49].

In the specific context of wood, the shrinkage across the grain direction can be four times higher than along the grain, thus explaining the preferential cracking of wood across the grain [50]. Therefore, it can be useful to represent the volumetric shrinkage ratio γ as a function of the linear shrinkage contribution $\gamma_\parallel$ along the grain, and $\gamma_\perp$ perpendicular to the grain as

$$\gamma = \gamma_\parallel \gamma_\perp^2 \ . \tag{6}$$

2.3. Measurements of solid density

The fundamental property that enables the simultaneous imaging of the gas-phase temperature and the biomass pyrolysis via XCT is the large separation in attenuation values μ between biomass, char, and Kr diluent. This separation allows a direct segmentation between the three regions [40]. The gas and solid phases are separated by thresholding. The solid phase is modeled as a mixture of virgin biomass and pyrolyzed char. Therefore, using the char volume fraction X_c, any intensive solid property ϕ_s is locally given by

$$\phi_s = (1 - X_c)\phi_b + X_c\phi_c \ , \tag{7}$$

in which ϕ_b corresponds to the quantity in the virgin biomass and ϕ_c is that in the region of pure char. ϕ_s can be the solid density ρ_s, the solid porosity ϵ_s, or the solid linear attenuation μ_s.

Because biomass materials feature porosities above 50%, both the solid material and the Kr within the pores attenuate the X-rays. However, since the X-ray resolution is only 300 μm, the biomass pores are not individually resolved. Instead, the attenuation signal for a given pixel corresponds to the volume-average of the two phases, such that the linear attenuation measured within the solid region can be expressed as

$$\mu = \mu_s + \epsilon_s\mu_{\text{Kr}}(T_g^\epsilon, X_{\text{Kr}}^\epsilon) \ , \tag{8}$$

in which μ_s represents the solid contribution to the attenuation, ϵ_s is the porosity, and $\mu_{\text{Kr}}(T_g^\epsilon, X_{\text{Kr}}^\epsilon)$ is the attenuation of Kr that is present within the solid internal pore volume at a gaseous temperature T_g^ϵ and volume fraction X_{Kr}^ϵ. In the absence of Kr, the solid contribution μ_s is the only source of X-ray attenuation. Using Eq. (7) for the linear attenuation μ_s, the char volume fraction X_c can be determined as

$$X_c = \frac{\mu_b - \mu_s}{\mu_b - \mu_c} \ . \tag{9}$$

In the presence of Kr in the internal pore volume of the solid, it is not possible to isolate the solid contribution μ_s from the measured signal μ without further information. However, at the mean X-ray energy of 42 keV used in this work, the Kr attenuation is significantly smaller than the attenuation by the solid. Therefore, a first approach consists in neglecting the inner-pore Kr contribution, as was done in previous work [40].

An alternative approach is proposed here. By assuming a homogeneous Kr volume fraction, the temperature of the submerged gas-phase is approximated by a thermocouple reading, and Eq. (8) is used to determine the solid attenuation μ_s. Combining Eq. (7) for the porosity with Eqs. (8) and (9) thus results in the following equation used to determine the solid attenuation by the porous matrix:

$$\mu_s = \frac{\mu(\mu_b - \mu_c) - \mu_{\text{Kr}}(\mu_b\epsilon_c - \mu_c\epsilon_b)}{\mu_b - \mu_c - (\epsilon_c - \epsilon_b)\mu_{\text{Kr}}} \ . \tag{10}$$

The char volume fraction and solid density are subsequently determined using Eqs. (9) and (7). A discussion of the uncertainties provided as supplementary material estimates errors of up to 10% for the density measurements. The values for linear attenuation and density for biomass and char were determined from initial scans of pristine biomass samples, and final scans of char samples with complete pyrolysis. To evaluate the density, the total solid volume V_s was measured by counting the volumetric pixels, or voxels, within the solid region. To determine the biomass porosity ϵ_b, two scans were acquired at the beginning of each experiment. The first scan was performed without Kr in the flow, such that μ_s was directly measured, while in the second scan, Kr was added to the flow at a known volume fraction. By difference, the Kr attenuation term in Eq. (8) was isolated, from which the porosity was determined. To evaluate the char porosity, the same procedure was repeated at the end of each experiment with complete pyrolysis. This technique was previously employed to measure the porosity of shale rocks [51], and further details about the method and Kr adsorption are provided in a separate study [52].

2.4. Gas-phase temperature measurements

Due to the large density differences between solid and gas phases, values for the linear attenuation μ significantly differ between the two phases [40]. As a result, segmentation of the two phases using a global threshold is a robust way to separate the gas-phase from the solid material. A threshold value of $\mu_t = 0.025$ cm^{-1} was used in this work, which was obtained as the average of the values obtained using Otsu's method across the different materials.

To obtain adequate contrast in the gas-phase, gaseous N_2 is replaced with Kr [43]. By assuming an ideal gas and an isobaric system, the Kr attenuation at a given gas-phase temperature T_g and Kr volume fraction X_{Kr} can then be determined as [40,43]

$$\mu_{\text{Kr}}(T_g, X_{\text{Kr}}) = \mu_{\text{Kr,ref}}\frac{T_{g,\text{ref}}}{T_g}\frac{X_{\text{Kr}}}{X_{\text{Kr,ref}}} \ , \tag{11}$$
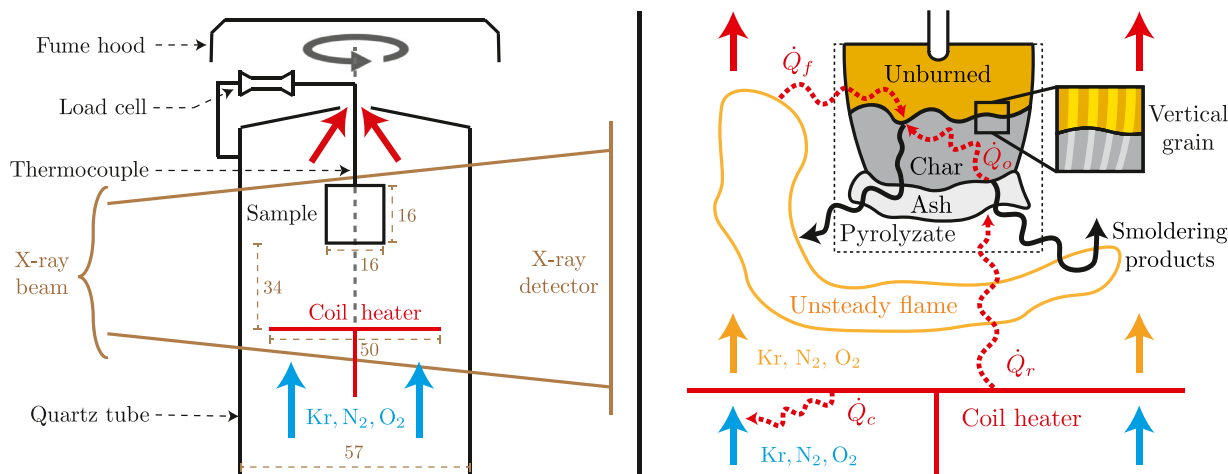
(a) Schematic of the experimental setup placed inside the X-ray system. Dimensions are given in millimeters.

(b) Schematic of the physical processes occurring within and around the biomass samples during combustion.

Fig. 1. Schematics of the experimental configuration showing (a) the table-top instrument, and (b) the physical processes.

in which the subscript 'ref' refers to a known reference state. For a constant Kr volume fraction, T_g can thus be inferred from the measured μ-values. Because of the inverse dependence between μ_{Kr} and T_g, uncertainties in temperature scale quadratically with respect to temperature. Therefore, up to 15% uncertainties are estimated at 2000 K, even though these uncertainties remain below 2% at 300 K. Besides, the release of volatile gases near the sample surface reduces X_{Kr} locally. This effect is quantified in the supplementary material, showing that a maximum overall reduction of 3% can be expected.

3. Experimental setup

3.1. Experimental configuration and flow conditions

Multiple cubic wood samples were instrumented inside of a quartz tube that was ventilated with a mixture of Kr, N_2 and O_2, as schematically represented in Fig. 1a. Heating was provided to the flow and the sample using a flat coil heater. The coil heater was placed 34 mm below the bottom of the unburned sample, had an outer diameter of 50 mm, and consisted of a flat spiral of nichrome wire of 0.51 mm diameter (AWG gauge 24). The wire was submitted to a voltage of 26.4 V, for a total dissipated heat of 158 W. The incident flow was heated by convection to a temperature T_∞ of 950 ± 100 K right above the heater, as measured by XCT. At this temperature, a convective heat transfer coefficient of 9.0 W/m²K was computed from empirical Nusselt correlations for a sphere of equivalent volume heated in a laminar buoyant flow [52]. This value increased to 15 W/m²K for a flow temperature of 2000 K, representative of the flaming conditions.

Figure 1b is a schematic of the physical processes occurring during combustion. The sample is heated by radiation $\dot{Q}_r$ and convection $\dot{Q}_c$ from the coil heater, and the pyrolysis is sustained by the additional heat released by char oxidation $\dot{Q}_o$ and flaming $\dot{Q}_f$. The convective heating $\dot{Q}_c$ corresponds to 24% of the 158 W power provided to the heater. This contribution was computed from the amount of heat required to bring the mixture from 300 K to 950 K. To compute the radiative heating $\dot{Q}_r$ on the sample, a view factor of 1.11% was determined by using the analytic formula for two coaxial disks of unequal diameter [53]. Assuming no heat loss, the incident radiation provided to the lower surface of the sample was evaluated as 5.23 kW/m². This upper bound corresponds to the value of

the radiation at the initial distance of 34 mm from the disc heater. Given the 650 K temperature difference measured between the averaged sample thermocouple reading of 550 K and the measured coil heater temperature of 1200 K, the effective heat transfer coefficient for radiation was evaluated to 8.0 W/m²K.

The quartz tube in which the sample was placed had an inner D diameter of 57 mm, an outer diameter of 61 mm, and a height of 300 mm. The gas mixture was supplied 200 mm below the sample from the bottom of the quartz tube. The mixture of Kr, N_2 and O_2 was supplied from four gas cylinders containing air, pure N_2, pure Kr and a mixture of 21% O_2 per volume balanced with Kr. Mass flow controllers from Alicat Scientific were used to provide a constant flow rate of 2.89 ± 0.12 liter per minute. The O_2 mole fraction X_{O_2} was varied from 0 to 0.21, while keeping a constant Kr mole fraction of 0.50. The vertical bulk velocity U of the flow within the quartz tube was kept constant at a value of 1.89 ± 0.08 cm/s. Over the range of different O_2 concentrations, the density was evaluated as 2.29 ± 0.02 kg/m³. The Froude number, $Fr = U/\sqrt{gD}$, was equal to 0.027, indicating an unsteady flow dominated by buoyancy. The gas-phase temperature measurements reported in this work should thus be interpreted as time-averaged values. It was verified experimentally via XCT that the surrounding air did not penetrate within the tube from the top, thus preserving the uniform Kr environment.

3.2. Biomass samples

The biomass samples investigated were cubes of $L = 16.0 \pm 0.1$ mm side made out of four different wood types. These types consisted of one softwood, douglas fir, and three hardwoods, namely birch, walnut, and oak. Pictures of several samples of birch and douglas fir before and after combustion are presented in Fig. 2a. Figure 2b presents microscopic images of the different materials, highlighting the variety in grain structure, pore size, and regularity. The samples were machined into cubes from commercial lumber, while keeping the wood grain direction parallel to one of the cube edges. The samples were centered within the quartz tube and held vertically via a K-type thermocouple. The thermocouple was press-fit 2–4 mm deep into a hole of 3 mm diameter drilled in the center of the top surface of the sample. A load cell held the thermocouple in place, providing instantaneous mass measurements of the sample with about 50 mg accuracy. The grain direction was kept parallel to the flow, except for birch, for which

E. Boigné, N.R. Bennett, A. Wang et al.
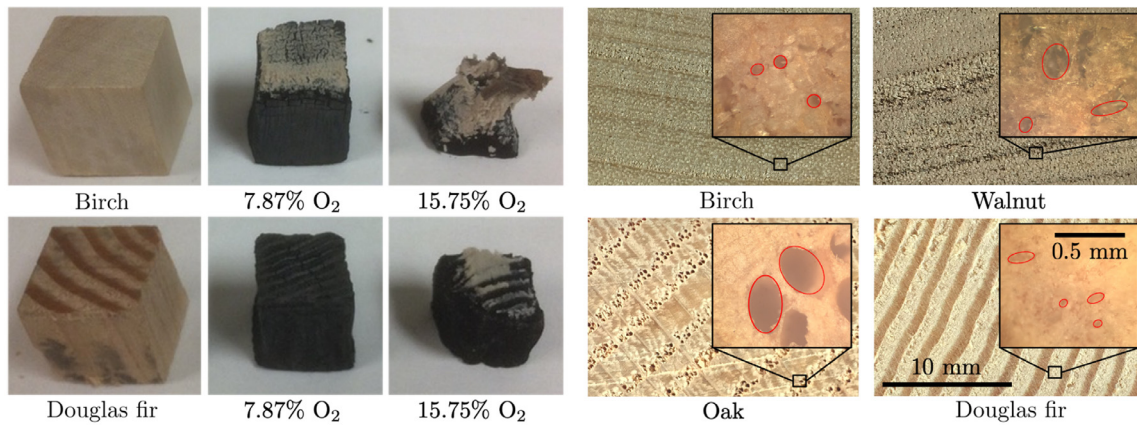
(a) Sample pictures: (left) unburned materials, and burned ma- (b) Material surfaces with optical microscopy inset images
terials operated at (center) 7.87% O_2, and (right) 15.75% O_2. (10×). Wood grain is perpendicular to the plane of the page.

Fig. 2. Samples: (a) pictures for birch and douglas fir, and (b) close-up images of the material surfaces.

Table 1
Characterization of the different wood samples studied, reporting mass-loss and sample mass after 3-hour drying at 110°C, Lower Heating Value (LHV), Higher Heating Value (HHV), proximate analysis, and ultimate analysis after drying. Mean values are reported with inter-sample standard deviation.

Biomass type	Birch	Walnut	Oak	Douglas Fir
Softwood / Hardwood	Hardwood	Hardwood	Hardwood	Softwood
Mass loss after 110°C drying [wt %]	6.86 ± 0.63	6.04 ± 0.90	6.64 ± 0.64	8.84 ± 0.95
Sample mass after 110°C drying [g]	2.32 ± 0.23	1.82 ± 0.07	2.46 ± 0.09	2.24 ± 0.10
Biomass LHV [MJ/kg]	16.4	16.9	16.6	16.1
Biomass HHV [MJ/kg]	17.8	18.2	17.9	17.5
Biomass proximate analysis [wt %]				
Moisture content	3.54 ± 0.01	3.47 ± 0.01	3.31 ± 0.04	3.21 ± 0.01
Volatile matter	82.45 ± 0.04	78.73 ± 0.16	79.54 ± 0.11	80.89 ± 0.16
Fixed carbon	13.81 ± 0.03	17.17 ± 0.16	16.87 ± 0.13	15.83 ± 0.20
Ash	0.20 ± 0.02	0.63 ± 0.01	0.28 ± 0.03	0.08 ± 0.050
Biomass ultimate analysis [wt %]				
Carbon	47.6	47.8	46.3	48.8
Oxygen	45.6	45.2	47.1	44.7
Hydrogen	6.34	6.14	6.10	6.35
Nitrogen	< 0.20	< 0.20	< 0.20	< 0.20
Sulfur	0.10	0.10	0.14	0.09
Theoretical attenuation ζ_b^{th} [cm^2/g]	0.246	0.245	0.247	0.245

both perpendicular ($\perp$) and parallel ($\parallel$) grain orientations were studied. After machining, the samples were dried for three hours at 110°C and stored in a desiccator. Table 1 provides results from different material tests performed after drying. The heating values and the results of the proximate and ultimate analyses are similar for the materials considered. The supplementary material reports the detailed TGA measurements, and histograms of material density measured via XCT.

3.3. X-ray system and acquisition procedure

The X-ray absorption measurements were performed using a tabletop laboratory scanner. The cone-beam setup is shown in Fig. 1a and consists of a X-ray tube, a rotating table on which the sample instrument is placed, and a flat X-ray detector. Further details on this setup can be found in previous studies [40,43,54]. The focal spot had a nominal size of 0.3 mm and the detector had a uniform pixel size of 194 μm. The distance between the focal spot and the detector was of 64.2 ± 0.3 cm. The rotating table was placed at a distance of 45.1 ± 0.2 cm from the source, for a geometric magnification of 1.42. These distances were measured via a standardized calibration procedure used for alignment [55]. The tube was operated at 60 kV and 23 mA, chosen as a trade-off

between maximizing signal-to-noise ratio and minimizing thermal load on the filament. X-ray photons were generated by pulses at a frequency of 7.5 Hz. Each fluoroscopy pulse lasted 40 ms, which was synchronized with the detector exposure time.

For each sample, the experiment consisted in the successive acquisitions of 19–21 XCT scans taken *in-situ*, while the sample was burning. One scan corresponded to 225 projection images acquired over a 30-second period, during which the sample was rotated by 360°. The experiments started at time $t = 00:00$ at which the sample was placed within the tube, after the flow and heater had reached steady state. The first *in-situ* scan was started 15–35 s later, after which successive scans were acquired every 70–90 s. At time $t = 16:00 \pm 00:30$, after 13–15 scans, the heater was turned off and successive scans were acquired to image the cooling phase of the burned sample. Before and after each experiment, the quartz tube without sample and any flow was imaged, and these calibration scans were subtracted from each scan to remove the attenuation from the quartz tube and thermocouple. Dark field calibrations were acquired between each scan to reduce after-glow artifacts, whereas flat field calibrations were performed before and after each experiment [43].

Each image represents a 2D array of line-integrals $\int \mu(l)\,dl$ as defined in Eq. (1). By collecting the images acquired during one

ARTICLE IN PRESS

JID: CNF   [m5G;September 18, 2021;19:6]

E. Boigné, N.R. Bennett, A. Wang et al.   Combustion and Flame xxx (xxxx) xxx

Table 2

Operating conditions reported in this work, indicating for each biomass and oxygen mole fraction X_{O_2} the nomenclature used and the regime observed corresponding to pure pyrolysis (P), smoldering without flaming (S), and flaming followed by smoldering (F). The grain orientation was either parallel ($\parallel$) or perpendicular to the vertical flow direction ($\perp$).

Biomass	X_{rmO_2} [%]					
	0.00	5.25	7.87	10.50	15.75	21.00
Birch $\parallel$	B0 (P)	B5 (S)	B8 (F)	B10 (F)	B16 (F)	B21 (F)
Birch $\perp$	B0$\perp$ (P)	B5$\perp$ (S)	B8$\perp$ (S)	B10$\perp$ (F)	B16$\perp$ (F)	-
Walnut $\parallel$	W0 (P)	W5 (P)	W8 (S)	W10 (F)	W16 (F)	-
Oak $\parallel$	O0 (P)	O5 (P)	O8 (P)	O10 (F)	O16 (F)	-
Douglas Fir $\parallel$	D0 (P)	D5 (P)	D8 (F)	D10 (F)	D16 (F)	-

Table 3

Material properties calculated from XCT-data. Mean values are reported with inter-sample standard deviation.

Biomass type	Birch	Walnut	Oak	Douglas Fir
Material density ρ_b [kg/m^3]	566 ± 55	444 ± 18	601 ± 22	546 ± 24
Material porosity ϵ_b [%]	56.0 ± 0.4	63.4 ± 0.2	46.6 ± 0.8	51.8 ± 0.8
Material attenuation ζ_b [cm^2/g]	0.212 ± 0.006	0.213 ± 0.002	0.205 ± 0.003	0.208 ± 0.003
Char density ρ_c [kg/m^3]	267 ± 24	222 ± 20	263 ± 6	247 ± 18
Char porosity ϵ_c [%]	78.8 ± 1.4	80.9 ± 2.6	76.6 ± 1.1	78.2 ± 1.6
Char attenuation ζ_c [cm^2/g]	0.135 ± 0.006	0.131 ± 0.010	0.163 ± 0.004	0.153 ± 0.011
Effective volatile matter Y_p [wt %]	67.5	68.1	69.2 ± 3.6	69.7
Volume shrinkage ratio γ [%]	68.9 ± 2.6	63.8 ± 3.0	70.4 ± 1.2	67.0 ± 3.7
Volume shrinkage parameter χ	1.28 ± 0.13	1.36 ± 0.13	1.23 ± 0.04	1.27 ± 0.09

scan at different angles, the 3D field of linear attenuation $\mu(\mathbf{x})$ was reconstructed for each scan. Tomographic reconstruction was performed with an isotropic voxel size of 136 μm using the Astra toolbox implementation of the Feldkamp-Davis-Kress (FDK) algorithm [56,57]. Because each acquisition lasted 30 s, the attenuation field corresponds to the average over that 30-second period. At the maximum burning rate measured of about 0.9 g/min, the front propagation speed is approximately 7.0 mm/min. Therefore, material changes occurred over up to 25 voxels within the solid during the 30-second acquisition, resulting in blurring of the results for scans with high burning rates.

3.4. Operating conditions

Four different types of biomass samples were examined and two grain orientations were investigated for the birch. While keeping the flow velocity and Kr concentration constant, the flow oxygen concentration was also varied. The different operating conditions investigated experimentally are summarized in Table 2, detailing the nomenclature and the combustion regimes observed. At low oxygen content, pure pyrolysis (P) was observed. This regime corresponds to experiments in which the rate of oxidation measured with XCT remained lower than 0.01 g/min [40]. At slightly higher oxygen concentrations, sustained smoldering regimes (S) were identified from the larger rates of oxidation measured. In these regimes, gas-phase ignition was not observed. At the highest oxygen concentrations, the gas-phase ignited within the first few minutes of the experiment, resulting in a flaming regime (F). The flaming lasted for 4 to 6 minutes, and was followed by sustained smoldering. The gas-phase ignition and extinction times were identified by visually monitoring the presence of a flame through the transparent quartz tube.

4. Results

Experimental results are presented in this section for selected operating conditions from Table 2. Values of density, porosity, and attenuation are reported in Table 3 for each material. Fuel consumption measurements and cross-sections of solid density and
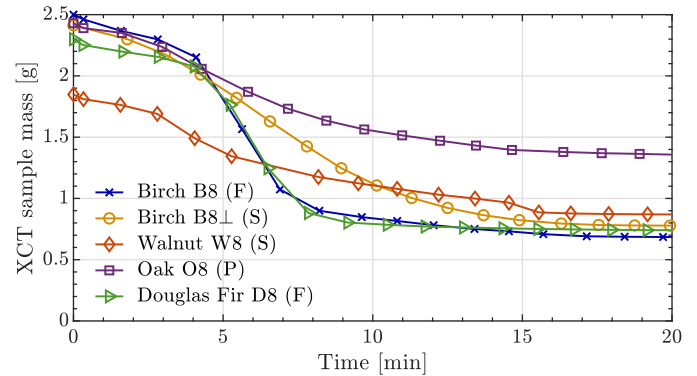

Fig. 3. Sample mass inferred from XCT over the duration of the experiment for different materials at 7.87% O$_2$. Each marker corresponds to one XCT acquisition.

gas temperature are then compared for different materials and grain orientations. The internal pyrolysis and oxidation reactions are later analyzed by investigating 1D spatial profiles of solid density. Finally, measurements of the volume shrinkage are discussed.

4.1. Fuel consumption measurements

The fuel consumption measured by XCT is presented in Fig. 3 for different materials at an oxygen concentration of 7.87%. The sample mass was obtained by integrating the solid density over the sample volume at each timestep. At these conditions, regimes of flaming were observed for birch and douglas fir, smoldering without flaming for walnut, and pure pyrolysis for oak. These measurements show that materials with similar composition, as determined by proximate and ultimate analysis, can feature large variations in their reaction rate. These results thus suggest that models of biomass combustion should account for the millimeter-scale fuel structure.

Depending on the characteristic times of heat transfer and reactions, different asymptotic pyrolysis regimes can be identified [45,58]. In the present configuration, the total external heat
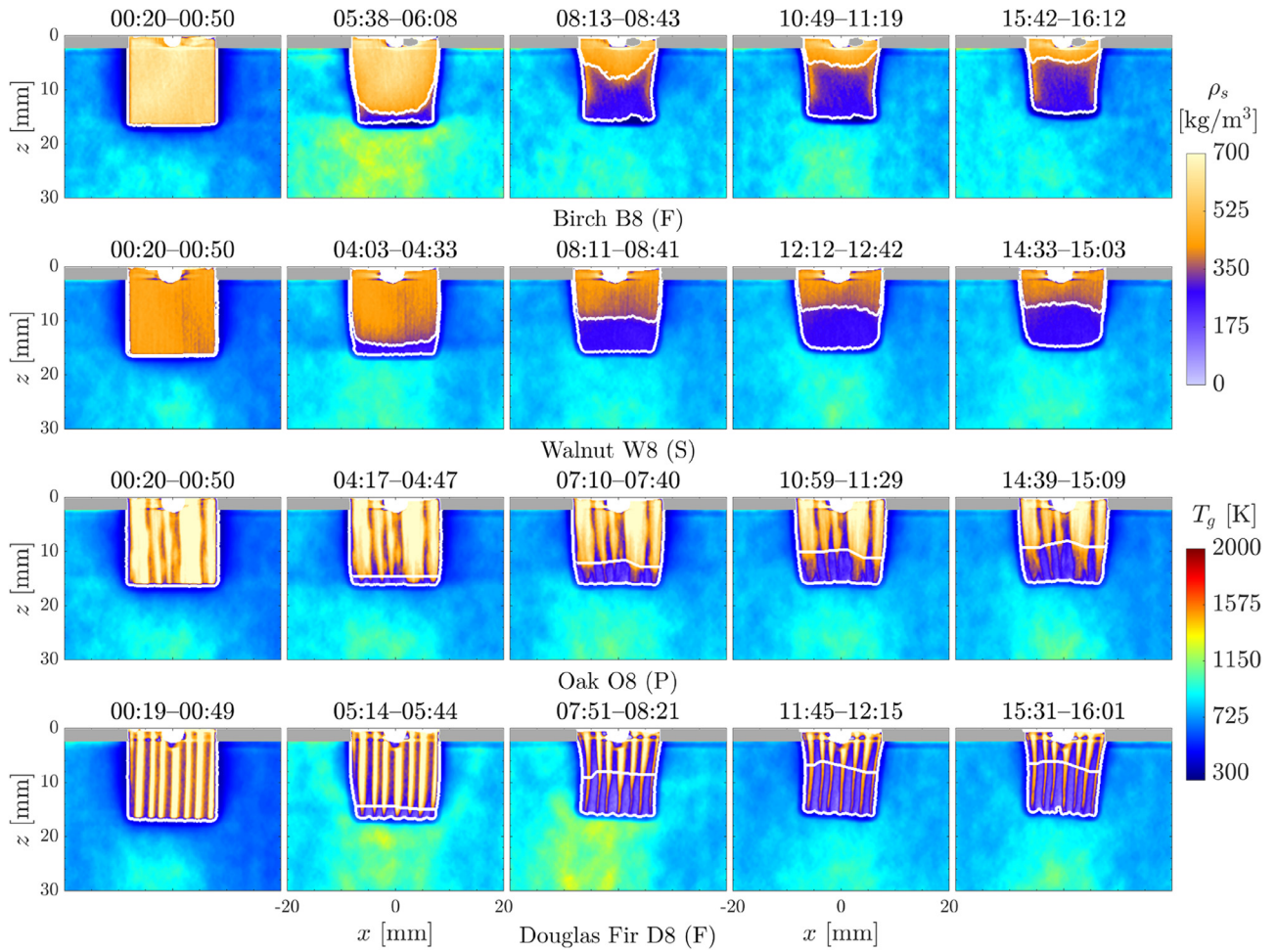
Fig. 4. XCT measurements showing vertical cross-sections at $y = 0$ of simultaneous gas temperature and solid density for conditions B8 (F), W8 (S), O8 (P), and D8 (F). White contours indicate the pyrolysis and oxidation fronts.

transfer coefficient ranged from $h = 17$ W/m^{2}K without flaming, to $h = 23$ W/m^{2}K during flaming. The Biot number Bi$= hL/\lambda$ is therefore evaluated to 1.6 for a mean h-value of 20 W/m^{2}K, and a thermal conductivity $\lambda = 0.2$ W/mK, typical of birch biomass [59]. This value for Bi indicates that temperature gradients within the sample cannot be neglected and that the thermocouple reading at the top of the sample differs from the temperature at the oxidation surface.

To discuss the combustion regime, a characteristic pyrolysis time τ_p can be evaluated from the experimental measurement of the pyrolyzate mass m_p as $\tau_p = m_p/\dot{m}_p$. For the conditions shown on Fig. 3, measured τ_p values range from 4 min for douglas fir to 15 min for oak [52]. This time can be compared to characteristic heat transfer times by conduction τ_c and external heating τ_h defined as

$$\tau_c = \frac{\rho_b c_{p,b} L^2}{\lambda} \qquad \qquad \tau_h = \frac{\rho_b c_{p,b} L}{h} , \qquad (12)$$

in which $c_{p,b}$ is the heat capacity of the biomass. With a value $c_{p,b} = 1.42$ J/gK taken from the literature for birch [59], the characteristic conduction and external heating times are evaluated to 17 and 11 min, respectively. At the fastest conditions investigated in this work, the pyrolysis therefore tends towards having a narrow reaction front whose propagation is governed by the internal heat transfer [58]. In contrast, at the slowest pyrolysis conditions observed, the progress of the process tends to be more controlled by the kinetics, and occur over a broader reaction front.

Similar calculations can be performed for the char oxidation re-action within the sample after pyrolysis. Because of the decrease in material density, heat conductivity, and heat capacity [59], the heating times are reduced by factors of 2–4. For this case, the ox-idation reaction times measured experimentally range between 10 and 60 min, thus indicating regimes more controlled by the ki-netics. Although these calculations provide insights on the range of regimes investigated, it is noted that because of the high Biot number, none of the conditions observed fall within the reported ranges of asymptotic models [58]. The conditions investigated are instead more representative of general distributed processes in which coupled heat transfer and kinetics control the progress of the reaction.

4.2. 3D measurements of temperature and density

From the XCT measurements, the gas-phase temperature and solid-phase density are simultaneously retrieved over time. Cross-sections for center-slices at $x = 0$ and $y = 0$ of the sample are pre-sented in Fig. 4 for different materials, and in Fig. 5 for different grain orientations. In these figures, the pyrolysis front, shown in white, is defined using the convex hull of the isocontour of solid attenuation μ_s at values ranging from 0.045 to 0.085 cm^{-1}, de-pending on the material. Note that the actual pyrolysis front is thicker than the white curve, and a different choice of the thresh-old can highlight a fingering of the pyrolysis front [40].
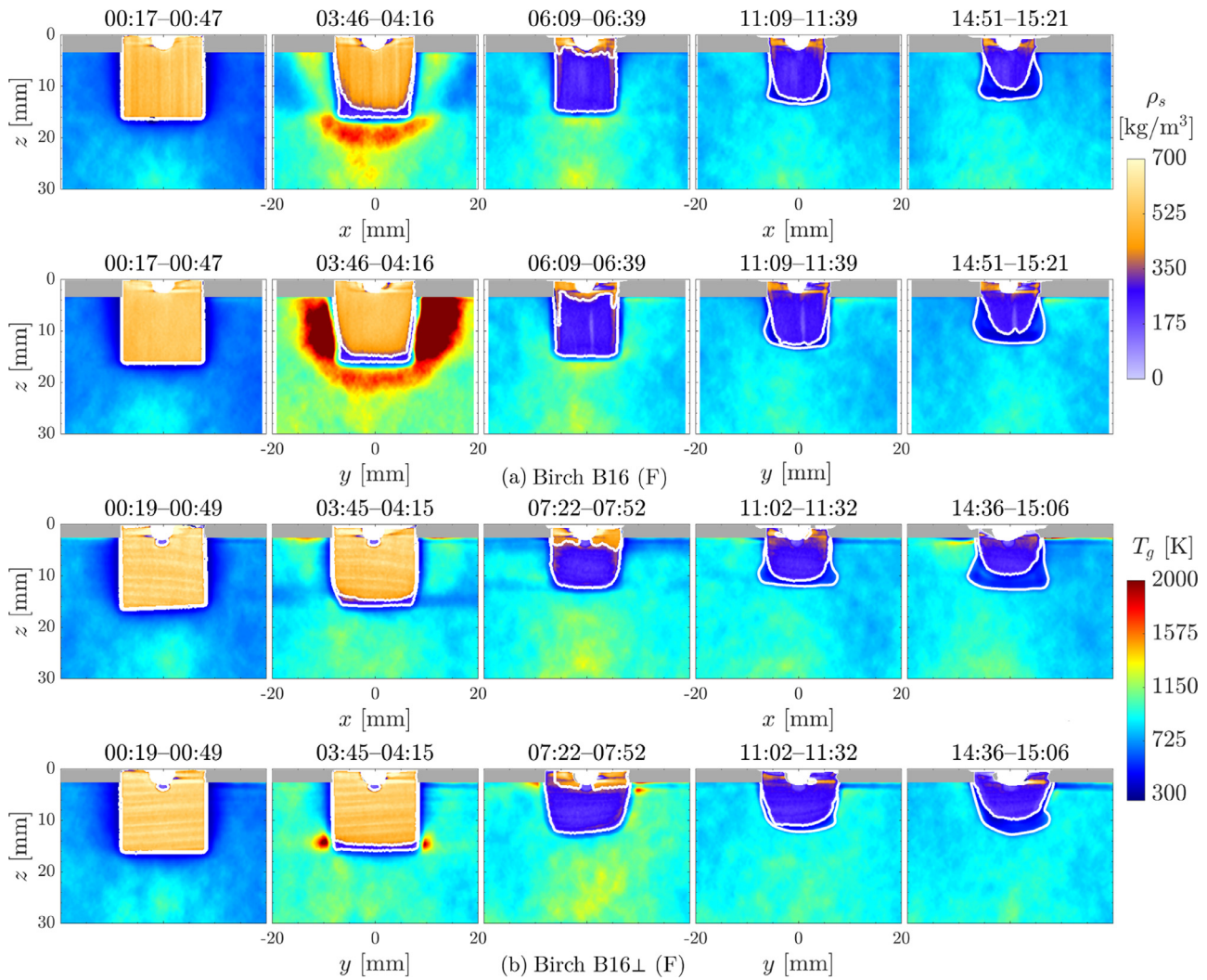
Fig. 5. XCT measurements showing vertical cross-sections at $y = 0$ and $x = 0$ of gas temperature and solid density for (a) parallel grain orientation with porous micro-vessels aligned along the z-direction, and (b) perpendicular grain orientation with porous micro-vessels aligned along the y-direction. Flaming was observed in both cases: from 03:35 to 06:15 for the parallel grain, and from 04:15 to 09:20 for the perpendicular grain. Ash is delineated with a white line and is visible around the char in the last column for all cases.

As discussed in Section 2.1, the attenuation of ash is significantly higher than that of the organic content. When biomass combustion is completed, the only solid product left is ash. Therefore, the inorganic content initially distributed across the entire sample is concentrated in a thin layer at the solid surface as a result of the heterogeneous combustion. Because of the larger attenuation of minerals, these thin layers of ash are visible in the XCT measurements for experiments with high rates of char oxidation. This effect is particularly visible in the last column of Fig. 5, in which the ash regions are delineated by a white contour.

4.2.1. Influence of material type

The influence of the material type on the combustion behavior is presented in Fig. 4 for an oxygen concentration of 7.87%. Birch and walnut both have rather homogeneous density fields at the millimeter scale which is resolved with the X-ray measurements. Therefore, the pyrolysis is similar for both materials, despite birch being denser than walnut. With walnut, a lower pyrolysis rate and a lower gas-phase temperature are observed, which is explained by the absence of flaming. In contrast, oak and douglas fir are characterized by large density variations at the millimeter scale across the wood grain. This grain structure is irregular for oak and reg-

ular for douglas fir, which is characteristic of softwood materials. For both materials, although the density variations locally affect the burning rates, the propagation of the pyrolysis front remains similar to what is observed with birch and walnut.

4.2.2. Influence of grain orientation

For birch, two series of experiments were performed with the grain direction either vertical or horizontal. Figure 5 presents results comparing birch samples with vertical grain (B16) and horizontal grain (B16⊥) orientations, operated at 15.75% oxygen. Gas-phase ignition was observed in both cases. Even though the overall pyrolysis and oxidation rates remained comparable, flaming occurred earlier at a faster and more intense rate when the grain was aligned with the flow direction. However, the locations at which the flame anchored was clearly related to the grain orientation. For the case with parallel grain orientation, the porous microvessels of the wood are aligned vertically. When pyrolyzate gases are released under heat exposure, they are transported along these channels and thus ejected downward at the sample bottom. This mechanism results in the stabilization of the flame at the bottom of the sample, as is clearly visible on the $y = 0$ slices in Fig. 5. In contrast, for conditions in which the grain direction was horizontal,
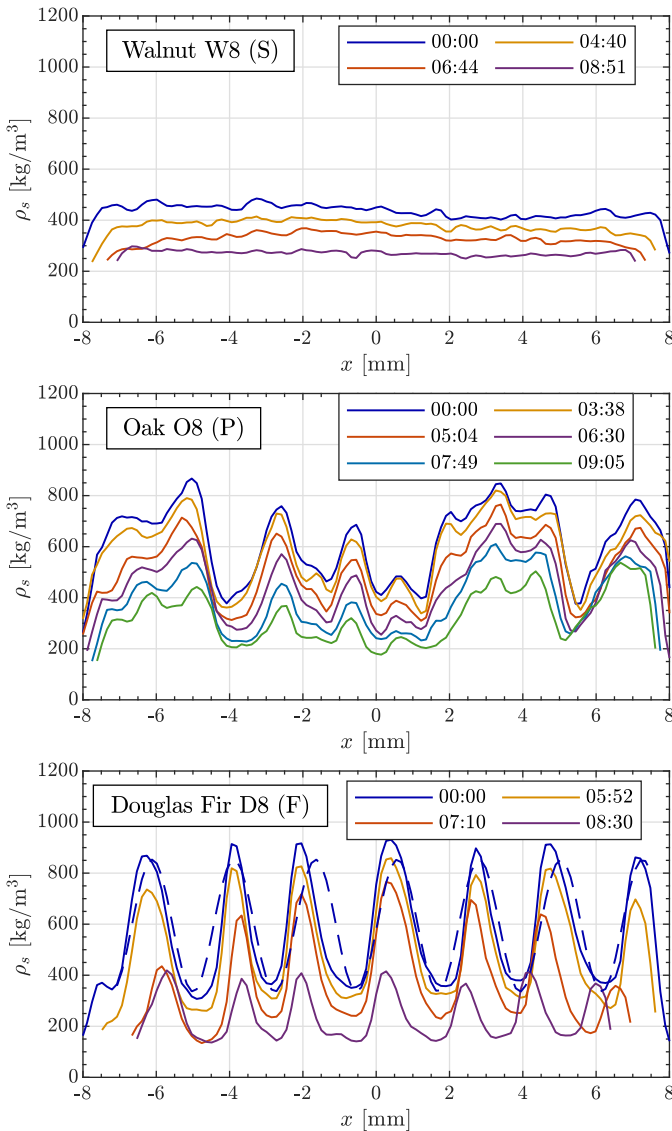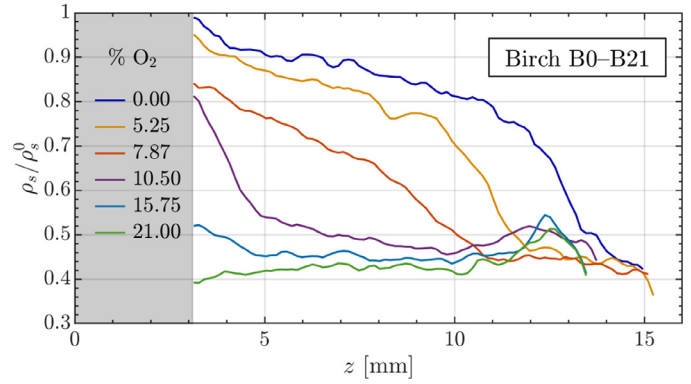
E. Boigné, N.R. Bennett, A. Wang et al.

Fig. 7. Normalized solid density profiles along the z-direction at centerline $x = 0$, $y = 0$, for parallel-grain birch with varied oxygen content (B0–B21) at time $08:30\pm00:30$. ρ_s^0 is the initial sample-averaged density for each case, equal to 571 ± 53 kg/m^3.

Fig. 6. Solid density profiles taken at $z = 12.4$ mm and $y = 0$ for different biomass samples at conditions W8, O8, and D8, from top to bottom. For douglas fir, the profile at time 00:00 is reasonably well represented by a sinusoidal function (dashed blue lines).

the flammable gas were released on the lateral sides of the sample at y-values of about ± 8 mm. The early flaming regime for the perpendicular grain orientation consisted of intermittent flames localized on these surfaces. This regime can be seen at $x = 0$ in Fig. 5. Besides, results from Fig. 3 show that the consumption rates may increase by a factor of three depending on the grain orientation. Therefore, the grain orientation is a fundamental property to accurately model biomass combustion and quantitatively predict heat release rates. In the context of wildfires, these results suggest that detailed biomass models require the consideration of the porous micro-structure within the fuel, as done in recent non-reactive simulations [25].

4.3. Reaction propagation for different materials

To compare the pyrolysis propagation for different materials, Figure 6 reports line profiles of solid density along the x-direction taken at $z = 12.4$ mm and $y = 0$ for conditions W8, O8, and D8 with 7.87% O$_2$. In Fig. 6, each line profile corresponds to a different

XCT scan. After the last scan presented for each case, changes remain below 2%, and the subsequent scans are not shown. The variations in material density is clear when considering unburned profiles. Walnut and birch have homogeneous density fields, whereas oak is characterized by an irregular density field, and results for douglas fir show regular variations across the grain, that are almost sinusoidal. For douglas fir, a dashed line indicates the density profile obtained with a sinusoidal function of mean 594 kg/m^3, amplitude 258 kg/m^3, and period 2.23 mm.

At this oxygen concentration, flaming was observed with douglas fir, but not with walnut and oak. As shown in the temperature cross-sections of Fig. 4, the presence of a flame increased the gas-phase temperature on the lateral sides of the sample, thereby resulting in further local heating. This added heating enhances the pyrolysis on the sides of the sample, as measured in the density profiles for douglas fir reported in Fig. 6. In contrast, for flameless conditions W8 and O8, the pyrolysis front remained mostly horizontal.

Whereas the pyrolysis occurs within the sample, the char oxidation is limited to a thin region near the surface of the sample. Figure 7 presents the normalized density along the z-direction extracted at time $08:30 \pm 00:30$ on the centerline $x = 0$ and $y = 0$ for conditions B0–B21. The density ρ_s is normalized by the initial sample-averaged density of each individual sample ρ_s^0. These results highlight the variations in thickness values of the pyrolysis front. Even though conditions B0, B5, and B8 cover three different combustion modes, similar density profiles are observed at time 08:30. At these conditions, a 10–20% density loss is observed at $z = 4$ mm, indicating that significant pyrolysis occurs even 1 cm deep within the sample. The shape of the pyrolysis front, and its larger spread with increasing O$_2$ concentration, are a consequence of heat conduction and the enhanced heat release at higher oxygen contents.

The pyrolysis was almost complete at 08:30 for the condition B10, while it had already completed for conditions B16 and B21. In the resulting pure char regions of the sample, the density reached a constant value for each case, except for a peak close to the lower surface. The formation of these peaks is attributed to the accumulation of more attenuating ash minerals at this location, and their width of 1–2 mm thus indicate the width of the char oxidation region.

4.4. Characterization of the volume shrinkage

In Table 3, mean values of the volume shrinkage parameters γ and χ are reported for different materials. These values were de-

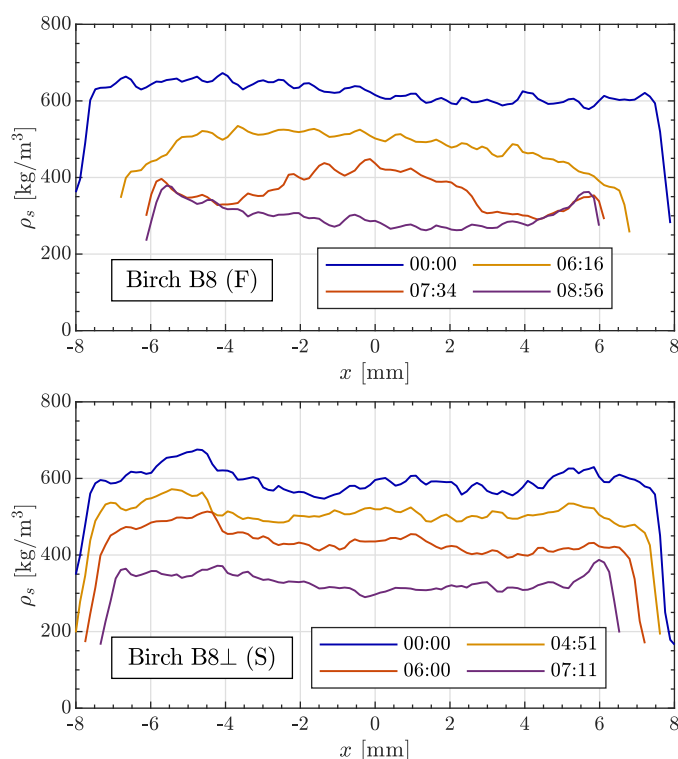**Fig. 8.** Solid density profiles taken at $z = 12.4$ mm and $y = 0$ for birch with parallel (B8) and perpendicular grain (B8⊥). For each case, the density profiles after the latest CT scan provided did not fluctuate any more than 2%.

termined using Eq. (4), in which the volatile content Y_p was measured from pyrolysis experiments for flow conditions with 0% oxygen. Despite the large structural discrepancies between the materials, values of 0.675 ± 0.04 are measured for all materials considered.

However, large variations are observed when comparing the volume reduction occurring along or across the grain. Figure 8 shows horizontal density profiles for birch at 7.87% oxygen, comparing the parallel and perpendicular grain orientations. The sample size reduction along the x-axis may be used to approximate the linear shrinkage ratio $\gamma_\perp$ for cases with vertical grain, and $\gamma_\parallel$ along the grain for case B8⊥. For instance, the width reduction from 16 to 12 mm (B8), and from 16 to 14 mm (B8⊥), represents shrinkage ratios $\gamma_\perp$ of 0.750, and $\gamma_\parallel$ of 0.875 for birch. A similar linear shrinkage along the grain $\gamma_\parallel$ of 0.86 can be measured along the z-axis profiles reported in Fig. 7 for condition B8. However, these linear shrinkage measurements over-estimate the volume reduction due to pyrolysis only, as the surface recess was augmented by the char oxidation at these conditions. Indeed, using the above values for $\gamma_\perp$ and $\gamma_\parallel$ would result in a volumetric shrinkage ratio of $\gamma = 0.492$ according to Eq. (6), a value significantly smaller than the 0.689 measured in pure pyrolysis (Table 3). Nonetheless, these results highlight that the shrinkage is more important across than along the grain. This trend is also apparent from Fig. 5, which presents thin and tall char pieces for parallel grain conditions, and wider and shorter ones for perpendicular grain orientations.

5. Conclusions

The dynamics of heterogeneous combustion were investigated for different solid biomass materials using *in-situ* X-ray Computed Tomography (XCT). The 3D fields of gas temperature and solid density were simultaneously measured during combustion for different oxygen concentrations. The grain orientation had a primary in-

fluence on the onset and stabilization of flaming, which increased the fuel consumption rate by up to a factor of three. Major variations in burning rates were also observed by varying the material type, even though thermogravimetric analysis showed that the materials considered had similar composition and chemical kinetics at the micro-scale. In contrast, the material physical properties and density distributions differed widely at the millimeter meso-scale. This work thus show that the material structure at the meso-scale is a fundamental factor to predict rates of fuel consumption and heat release in biomass combustion.

In addition, it was shown that XCT enables the detailed characterization of the volume shrinkage and the propagation of the pyrolysis and oxidation within the solid fuel. Specifically, the char oxidation was localized to a region of only 2 mm thickness near the surface, unlike the pyrolysis which was observed 1.5 cm within the sample. In the context of modeling and numerical simulations, these results demonstrate that XCT can thus provide quantitative information for material properties and detailed data that are resolved in space and time. These capabilities make XCT a promising measurement technique for *in-situ* characterization of material properties and combustion process in solid biomass.

For wildfire applications, it is relevant to understand meso-scale processes in order to better predict macro-scale dynamics. For instance, large-scale phenomena such as fire spotting and rekindle are governed by millimeter-scale ignitions from wind-borne ember or residual smoldering fuel [60]. Bench-scale experiments with detailed XCT measurements offer the ability to improve models of these local dynamics, thereby benefiting the predictive capabilities of overall wildfire spreads. In particular, measurements of the fuel shrinkage provides fundamental data for modeling, thereby complementing kinetic parametrisation obtained from TGA. The millimeter-scale material variations reported in this work also suggest that statistical models could better represent biofuel distribution in large-scale simulations. Finally, the simultaneous gas and density measurements highlighted the variability in combustion dynamics due to grain alignment, thus indicating that different models should be used to evaluate heat release rates of vertical tree trunks and leftover smoldering logs.

Declaration of Competing Interest

The authors declare that they have no known competing financial interests or personal relationships that could have appeared to influence the work reported in this paper.

Supplementary material

Supplementary material associated with this article can be found, in the online version, at doi:10.1016/j.combustflame.2021.111737.

References

[1] International Energy Association (IEA) database, 2018, (Available from: http://www.iea.org).

[2] K.T. Davis, S.Z. Dobrowski, P.E. Higuera, Z.A. Holden, T.T. Veblen, M.T. Rother, S.A. Parks, A. Sala, M.P. Maneta, Wildfires and climate change push low-elevation forests across a critical climate threshold for tree regeneration, Proc. Natl. Acad. Sci. 116 (13) (2019) 6193–6198, doi:10.1073/PNAS.1815107116. https://www.pnas.org/content/116/13/6193

[3] X.J. Walker, J.L. Baltzer, S.G. Cumming, N.J. Day, C. Ebert, S. Goetz, J.F. Johnstone, S. Potter, B.M. Rogers, E.A. Schuur, M.R. Turetsky, M.C. Mack, Increasing wildfires threaten historic carbon sink of boreal forest soils, Nature 572 (7770) (2019) 520–523, doi:10.1038/s41586-019-1474-y.

[4] L. Yermán, H. Wall, J. Torero, J.I. Gerhard, Y.L. Cheng, Smoldering combustion as a treatment technology for feces: sensitivity to key parameters, Combust. Sci. Technol. 188 (6) (2016) 968–981, doi:10.1080/00102202.2015.1136299.

[5] H.K. Wyn, M. Konarova, J. Beltramini, G. Perkins, L. Yermán, Self-sustaining smoldering combustion of waste: a review on applications, key parameters and potential resource recovery, Fuel Process. Technol. 205 (2020) 106425, doi:10.1016/j.fuproc.2020.106425.

[6] G.C. Scholes, J.I. Gerhard, G.P. Grant, D.W. Major, J.E. Vidumsky, C. Switzer, J.L. Torero, Smoldering remediation of coal-tar-contaminated soil: pilot field tests of STAR, Environ. Sci. Technol. 49 (24) (2015) 14334–14342, doi:10.1021/acs.est.5b03177.

[7] S.R. Kersten, X. Wang, W. Prins, W.P. Van Swaaij, Biomass pyrolysis in a fluidized bed reactor. Part 1: literature review and model simulations, Ind. Eng. Chem. Res. 44 (23) (2005) 8773–8785, doi:10.1021/ie0504856.

[8] P. Boulet, G. Parent, Z. Acem, T. Rogaume, T. Fateh, J. Zaida, F. Richard, Characterization of the radiative exchanges when using a cone calorimeter for the study of the plywood pyrolysis, Fire Saf. J. 51 (2012) 53–60, doi:10.1016/j.firesaf.2012.03.003.

[9] Z. Ghorbani, R. Webster, M. Lázaro, A. Trouvé, Limitations in the predictive capability of pyrolysis models based on a calibrated semi-empirical approach, Fire Saf. J. 61 (2013) 274–288, doi:10.1016/j.firesaf.2013.09.007.

[10] A.G. Barneto, J.A. Carmona, J.E. Alfonso, J.A. Ferrer, Use of thermogravimetry/mass spectrometry analysis to explain the origin of volatiles produced during biomass pyrolysis, Ind. Eng. Chem. Res. 48 (15) (2009) 7430–7436.

[11] J. Yang, H. Chen, W. Zhao, J. Zhou, TG-FTIR-MS study of pyrolysis products evolving from peat, J. Anal. Appl. Pyrolysis 117 (2016) 296–309.

[12] A.L. Brown, D.C. Dayton, M.R. Nimlos, J.W. Daily, Design and characterization of an entrained flow reactor for the study of biomass pyrolysis chemistry at high heating rates, Energy Fuels 15 (5) (2001) 1276–1285, doi:10.1021/ef010083k.

[13] C. Lautenberger, C. Fernandez-Pello, A model for the oxidative pyrolysis of wood, Combust. Flame 156 (8) (2009) 1503–1513, doi:10.1016/j.combustflame.2009.04.001.

[14] X. Huang, G. Rein, Thermochemical conversion of biomass in smouldering combustion across scales: the roles of heterogeneous kinetics, oxygen and transport phenomena, Bioresour. Technol. 207 (2016) 409–421, doi:10.1016/j.biortech.2016.01.027.

[15] M.A. Finney, J.D. Cohen, J.M. Forthofer, S.S. McAllister, M.J. Gollner, D.J. Gorham, K. Saito, N.K. Akafuah, B.A. Adam, J.D. English, R.E. Dickinson, Role of buoyant flame dynamics in wildfire spread, Proc. Natl. Acad. Sci. 112 (32) (2015) 9833–9838, doi:10.1073/pnas.1504498112.

[16] Y. Hu, E.G. Christensen, H.M. Amin, T.E. Smith, G. Rein, Experimental study of moisture content effects on the transient gas and particle emissions from peat fires, Combust. Flame 209 (2019) 408–417, doi:10.1016/j.combustflame.2019.07.046.

[17] V. Rebaque, I.S. Ertesvåg, R.F. Mikalsen, A. Steen-Hansen, Experimental study of smouldering in wood pellets with and without air draft, Fuel 264 (November 2019) (2020) 116806, doi:10.1016/j.fuel.2019.116806.

[18] H. Wang, P.J. Van Eyk, P.R. Medwell, C.H. Birzer, Z.F. Tian, M. Possell, Effects of oxygen concentration on radiation-aided and self-sustained smoldering combustion of radiata pine, Energy Fuels 31 (8) (2017) 8619–8630, doi:10.1021/acs.energyfuels.7b00646.

[19] A. Atreya, P. Olszewski, Y. Chen, H.R. Baum, The effect of size, shape and pyrolysis conditions on the thermal decomposition of wood particles and firebrands, Int. J. Heat Mass Transf. 107 (2017) 319–328, doi:10.1016/j.ijheatmasstransfer.2016.11.051.

[20] Y. Hu, W. Cui, G. Rein, Haze emissions from smouldering peat: the roles of inorganic content and bulk density, Fire Saf. J. 113 (December 2019) (2020) 102940, doi:10.1016/j.firesaf.2019.102940.

[21] R. Emberley, A. Inghelbrecht, Z. Yu, J.L. Torero, Self-extinction of timber, Proc. Combust. Inst. 36 (2) (2017) 3055–3062, doi:10.1016/j.proci.2016.07.077.

[22] S. Lin, X. Huang, Quenching of smoldering: effect of wall cooling on extinction, Proc. Combust. Inst. 38 (3) (2021) 5015–5022, doi:10.1016/j.proci.2020.05.017.

[23] B.V. Babu, A.S. Chaurasia, Heat transfer and kinetics in the pyrolysis of shrinking biomass particle, Chem. Eng. Sci. 59 (10) (2004) 1999–2012, doi:10.1016/j.ces.2004.01.050.

[24] M.J. Hagge, K.M. Bryden, Modeling the impact of shrinkage on the pyrolysis of dry biomass, Chem. Eng. Sci. 57 (14) (2002) 2811–2823, doi:10.1016/S0009-2509(02)00167-7.

[25] P.N. Ciesielski, M.F. Crowley, M.R. Nimlos, A.W. Sanders, G.M. Wiggins, D. Robichaud, B.S. Donohoe, T.D. Foust, Biomass particle models with realistic morphology and resolved microstructure for simulations of intraparticle transport phenomena, Energy Fuels 29 (1) (2015) 242–254.

[26] F. Richter, G. Rein, A multiscale model of wood pyrolysis in fire to study the roles of chemistry and heat transfer at the mesoscale, Combust. Flame 216 (2020) 316–325, doi:10.1016/j.combustflame.2020.02.029.

[27] F. De Souza Costa, D. Sandberg, Mathematical model of a smoldering log, Combust. Flame 139 (3) (2004) 227–238, doi:10.1016/j.combustflame.2004.07.009.

[28] O. Kadowaki, M. Suzuki, K. Kuwana, Y. Nakamura, G. Kushida, Limit conditions of smoldering spread in counterflow configuration: extinction and smoldering-to-flaming transition, Proc. Combust. Inst. 38 (3) (2021) 5005–5013, doi:10.1016/j.proci.2020.05.002.

[29] C. Lautenberger, C. Fernandez-Pello, Generalized pyrolysis model for combustible solids, Fire Saf. J. 44 (6) (2009) 819–839, doi:10.1016/j.firesaf.2009.03.011.

[30] S.D. Tse, R.A. Anthenien, A.C. Fernandez-Pello, K. Miyasaka, A novel application of ultrasonic imaging to study smoldering combustion, Combust. Flame 116 (1–2) (1997) 120–135. http://linkinghub.elsevier.com/retrieve/pii/S0010218098000534

[31] O. Putzeys, A. Bar-Ilan, G. Rein, A.C. Fernandez-Pello, D.L. Urban, The role of secondary char oxidation in the transition from smoldering to flaming, Proc. Combust. Inst. 31 (2) (2007) 2669–2676, doi:10.1016/j.proci.2006.08.006.

[32] D.H. Maylotte, C. Spiro, P.G. Kosky, E.J. Lamby, X-ray computed tomography of coal: final report, Technical Report, DOE/MC/19210-2357,, US Department of Energy, 1986, doi:10.2172/6339446.

[33] G.H. Fong, S. Jorgensen, S.L. Singer, Pore-resolving simulation of char particle gasification using micro-CT, Fuel 224 (March) (2018) 752–763, doi:10.1016/j.fuel.2018.03.117.

[34] J.P. Mathews, Q.P. Campbell, H. Xu, P. Halleck, A review of the application of X-ray computed tomography to the study of coal, Fuel 209 (February) (2017) 10–24, doi:10.1016/j.fuel.2017.07.079.

[35] R. Baettig, R. Rémond, P. Perré, Measuring moisture content profiles in a board during drying: a polychromatic x-ray system interfaced with a vacuum/pressure laboratory kiln, Wood Sci. Technol. 40 (4) (2006) 261–274, doi:10.1007/s00226-006-0068-7.

[36] A. Strandberg, M. Thyrel, N. Skoglund, T.A. Lestander, M. Broström, R. Backman, Biomass pellet combustion: cavities and ash formation characterized by synchrotron X-ray micro-tomography, Fuel Process. Technol. 176 (March) (2018) 211–220.

[37] K.J. Dobson, S.B. Coban, S.A. McDonald, J.N. Walsh, R.C. Atwood, P.J. Withers, 4-D imaging of sub-second dynamics in pore-scale processes using real-time synchrotron X-ray tomography, Solid Earth 7 (4) (2016) 1059–1073, doi:10.5194/se-7-1059-2016.

[38] K. Murai, T. Daitoku, T. Tsuruda, Three-dimensional analysis of the pyrolysis behavior of solid fuel by ultra high-speed X-ray CT, Proc. Combust. Inst. 38 (3) (2021) 3987–3994, doi:10.1016/j.proci.2020.08.026.

[39] B. Martin, J. Colin, P. Lu, M. Mounkaila, J. Casalinho, P. Perré, R. Rémond, Water migration in wood during imbibition assessed by X-ray imaging, E3S Web Conf. 172 (2020) 1–7.

[40] E. Boigné, N.R. Bennett, A. Wang, K. Mohri, M. Ihme, Simultaneous in-situ measurements of gas temperature and pyrolysis of biomass smoldering via X-ray computed tomography, Proc. Combust. Inst. 38 (3) (2021) 3899–3907, doi:10.1016/j.proci.2020.06.070.

[41] E. Boigné, N.R. Bennett, A. Wang, M. Ihme, Examining the effect of fire retardant on the combustion of wood via X-ray computed tomography, 12th U.S. National Combustion Meeting (2021).

[42] J. Als-Nielsen, D. McMorrow, Elements of modern X-ray physics, John Wiley & Sons, 2011.

[43] E. Boigné, P. Muhunthan, D. Mohaddes, Q. Wang, S. Sobhani, W. Hinshaw, M. Ihme, X-ray computed tomography for flame-structure analysis of laminar premixed flames, Combust. Flame 200 (2019) 142–154, doi:10.1016/j.combustflame.2018.11.015.

[44] J.H. Hubbell, S.M. Seltzer, Tables of X-ray mass attenuation coefficients and mass energy-absorption coefficients 1 keV to 20 MeV for elements $Z = 1$ to 92 and 48 additional substances of dosimetric interest, Technical Report, PB-95-220539/XAB; NISTIR-5632, National Institute of Standards and Technology, 1995.

[45] R.B. Bates, A.F. Ghoniem, Modeling kinetics-transport interactions during biomass torrefaction: the effects of temperature, particle size, and moisture content, Fuel 137 (2014) 216–229, doi:10.1016/j.fuel.2014.07.047.

[46] X. Ku, T. Li, T. Løvås, Effects of particle shrinkage and devolatilization models on high-temperature biomass pyrolysis and gasification, Energy Fuels 29 (8) (2015) 5127–5135, doi:10.1021/acs.energyfuels.5b00953.

[47] G. Caposciutti, H. Almuina-Villar, A. Dieguez-Alonso, T. Gruber, J. Kelz, U. Desideri, C. Hochenauer, R. Scharler, A. Anca-Couce, Experimental investigation on biomass shrinking and swelling behaviour: particles pyrolysis and wood logs combustion, Biomass Bioenergy 123 (August 2018) (2019) 1–13, doi:10.1016/j.biombioe.2019.01.044.

[48] I.T. Leventon, J. Li, S.I. Stoliarov, A flame spread simulation based on a comprehensive solid pyrolysis model coupled with a detailed empirical flame structure representation, Combust. Flame 162 (10) (2015) 3884–3895, doi:10.1016/j.combustflame.2015.07.025.

[49] M. Bellais, K.O. Davidsson, T. Liliedahl, K. Sjöström, J.B. Pettersson, Pyrolysis of large wood particles: a study of shrinkage importance in simulations, Fuel 82 (12) (2003) 1541–1548, doi:10.1016/S0016-2361(03)00062-0.

[50] K. Li, S. Hostikka, P. Dai, Y. Li, H. Zhang, J. Ji, Charring shrinkage and cracking of fir during pyrolysis in an inert atmosphere and at different ambient pressures, Proc. Combust. Inst. 36 (2) (2017) 3185–3194, doi:10.1016/j.proci.2016.07.001.

[51] B. Vega, A. Dutta, A.R. Kovscek, CT imaging of low-permeability, dual-porosity systems using high X-ray contrast gas, Transp. Porous Media 101 (1) (2014) 81–97, doi:10.1007/s11242-013-0232-0.

[52] E. Boigné, N.R. Bennett, A. Wang, M. Ihme, Quantitative X-ray computed tomography: prospects for the detailed in-situ imaging of bench-scale fire measurements,Under review (2021).

[53] J.R. Howell, M.P. Mengüç, R. Siegel, Thermal radiation heat transfer, CRC Press, 2015.

ARTICLE IN PRESS

JID: CNF   [m5G;September 18, 2021;19:6]

E. Boigné, N.R. Bennett, A. Wang et al.   Combustion and Flame xxx (xxxx) xxx

[54] J. Dunnmon, S. Sobhani, M. Wu, R. Fahrig, M. Ihme, An investigation of internal flame structure in porous media combustion via X-ray computed tomography, Proc. Combust. Inst. 36 (3) (2017) 4399–4408, doi:10.1016/j.proci.2016.06.188.

[55] S. Gao, W. Du, P. Balter, P. Munro, A. Jeung, Evaluation of IsoCal geometric calibration system for Varian linacs equipped with on-board imager and electronic portal imaging device imaging systems, J. Appl. Clin. Med. Phys. 15 (3) (2014) 164–181, doi:10.1120/jacmp.v15i3.4688.

[56] L.A. Feldkamp, L.C. Davis, J.W. Kress, Practical cone-beam algorithm, J. Opt. Soc. Am. A 1 (6) (1984) 612–619.

[57] W. van Aarle, W.J. Palenstijn, J. Cant, E. Janssens, F. Bleichrodt, A. Dabravolski, J.D. Beenhouwer, K.J. Batenburg, J. Sijbers, Fast and flexible X-ray tomography using the ASTRA toolbox, Opt. Express 24 (22) (2016) 25129–25147.

[58] D. Pyle, C. Zaror, Heat transfer and kinetics in the low temperature pyrolysis of solids, Chem. Eng. Sci. 39 (1) (1984) 147–158.

[59] S. Hostikka, A. Matala, Pyrolysis model for predicting the heat release rate of birch wood, Combust. Sci. Technol. 189 (8) (2017) 1373–1393, doi:10.1080/00102202.2017.1295959.

[60] M.A. Santoso, E.G. Christensen, J. Yang, G. Rein, Review of the transition from smouldering to flaming combustion in wildfires, Front. Mech. Eng. 5 (September) (2019) 49.